

Ti₃C₂T_x MXene Nanosheets as a Robust and Conductive Tight on Si Anodes Significantly Enhance Electrochemical Lithium Storage Performance

Mengting Xia,^{||} Bingjie Chen,^{||} Feng Gu, Lianhai Zu, Mengzhu Xu, Yutong Feng, Zhijun Wang, Haijiao Zhang,* Chi Zhang,* and Jinhu Yang*



Cite This: *ACS Nano* 2020, 14, 5111–5120



Read Online

ACCESS |



Metrics & More



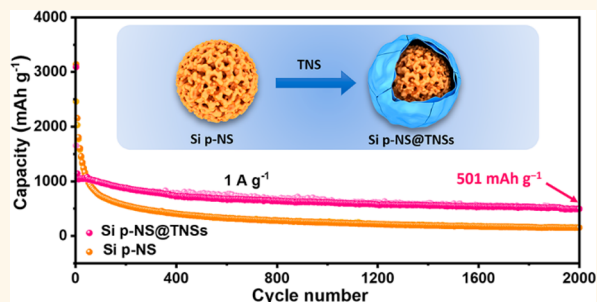
Article Recommendations



Supporting Information

ABSTRACT: Exploring Si-based anode materials with high electrical conductivity and electrode stability is crucial for high-performance lithium-ion batteries (LIBs). Herein, we propose the fabrication of a Si-based composite where Si porous nanospheres (Si p-NSs) are tightly wrapped by Ti₃C₂T_x (T_x stands for the surface groups such as –OH, –F) MXene nanosheets (TNSs) through an interfacial assembly strategy. The TNSs as a conductive and robust tight of the Si p-NSs can effectively improve electron transport and electrode stability, as revealed by substantial characterizations and mechanical simulations. Moreover, the TNSs with rich surface groups enable strong interfacial interactions with the Si p-NS component and a pseudocapacitive behavior, beneficial for fast and stable lithium storage. Consequently, the Si p-NS@TNSs electrode with a high Si content of 85.6% exhibits significantly enhanced battery performance compared with the Si p-NSs electrode such as high reversible capacity (1154 mAh g⁻¹ at 0.2 A g⁻¹), long cycling stability (up to 2000 cycles with a 0.026% capacity decay rate per cycle), and excellent rate performances. Notably, the Si p-NS@TNSs electrode-based LIB full cell delivers a high energy uptake of 405 Wh kg⁻¹, many-times higher than that of the Si p-NSs full cell. This work offers a strategy to develop advanced Si-based anode materials with desirable properties for high-performance LIBs.

KEYWORDS: MXene, silicon, structural stability, lithium-ion batteries, mechanical simulations



Lithium-ion batteries (LIBs) are the major power source for portable electronic devices and electrical/hybrid vehicles.^{1,2} However, graphite, the present commercial LIBs anode material, is insufficient to meet today's high energy demand due to its low theoretical specific capacity (372 mAh g⁻¹).^{3,4} Alternatively, silicon (Si) has attracted ever-increasing attention as one of the most promising anode materials for the next-generation LIBs thanks to its ultrahigh theoretical specific capacity (4200 mAh g⁻¹ for Li₂₂Si₅), suitable Li-uptake voltage (0.4 V vs Li/Li⁺), and natural abundance.^{5–9} However, the huge volume change (up to 400%) during cycling as well as the low intrinsic conductivity ($\approx 10^{-3}$ S cm⁻¹) and the low lithium diffusion coefficient (10^{-14} – 10^{-13} cm² s⁻¹) of Si anodes often cause electrode pulverization/crush and high reaction irreversibility,^{10–14} leading to permanent capacity loss and overall performance deterioration of batteries.

To overcome the deficiencies, carbon-based materials such as graphene with good conductivity and flexibility were often

addressed as the matrix for Si anode materials.^{15–19} In addition, to further relieve effect of volume change, Si components in the Si/graphene composites were usually designed at nanoscale with a variety of specific structures including nanoparticles, nanowires, nanotubes, nanosheets, and porous nanospheres.^{20–26} However, the surface of graphene bounded by sp² carbon without active polar groups shows a weak interaction with Si, resulting in an unstable interface between the two components of graphene and Si in the composites, which is adverse to the interfacial electron transfer and cycling stability.

Received: March 6, 2020

Accepted: April 9, 2020

Published: April 9, 2020



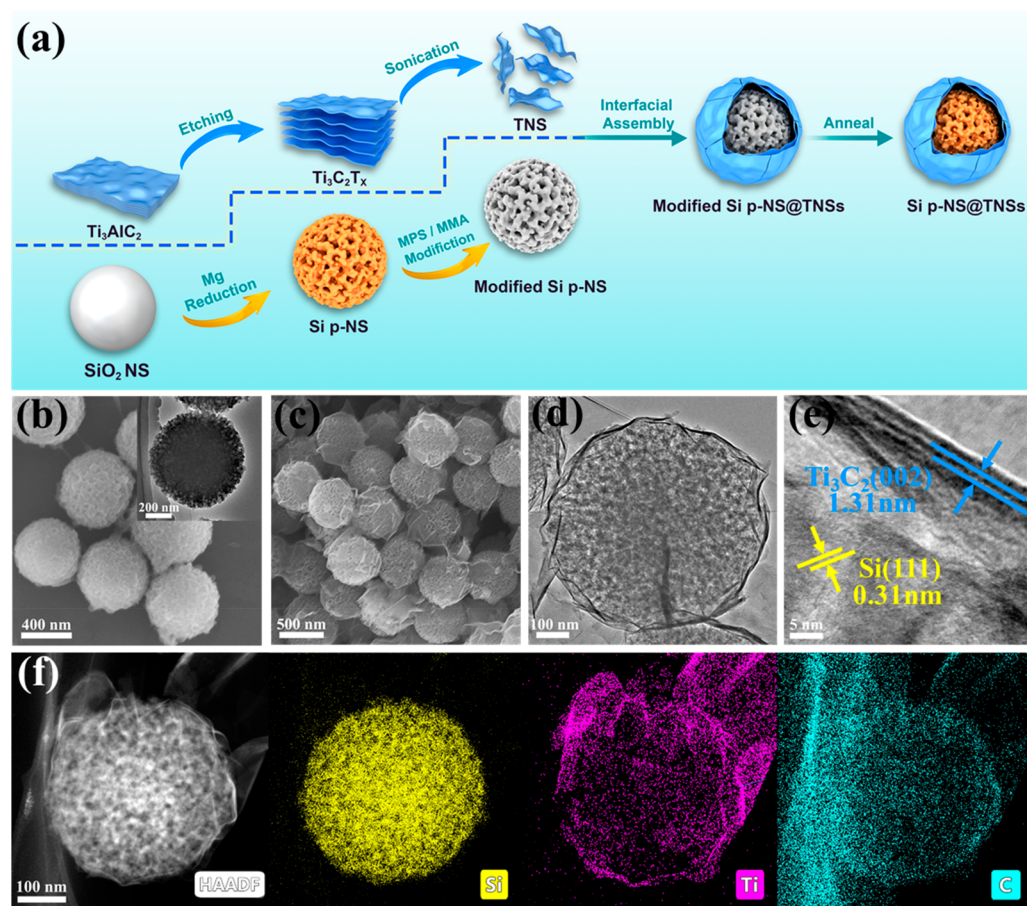


Figure 1. (a) Schematic illustration of the formation process of the Si p-NS@TNSs composite. (b, c) SEM images of the modified Si p-NSs coated with a (b) PMMA layer and the (c) Si p-NS@TNSs composite. The inset in panel b shows TEM image of a modified Si p-NS. (d, e) TEM and HRTEM images of the Si p-NS@TNSs composite. (f) Elemental mapping images of the Si p-NS@TNSs composite.

MXene, a new category of two-dimensional (2D) materials first reported in 2011 by Gogotsi and co-workers, has attracted more and more attention in the field of energy storage because of their unprecedented combinations of properties such as excellent electronic conductivity, high mechanical flexibility, and compositional adaptability.^{27–32} Titanium carbide ($\text{Ti}_3\text{C}_2\text{T}_x$) is a representative MXene material, showing a similar structure with graphene, but faster Li^+ transport ($\approx 10^{-10}$ – 10^{-9} $\text{cm}^2 \text{ s}^{-1}$) and higher charge/discharge rate due to the lower lithium diffusion barrier of Ti_3C_2 (0.07 eV) than that of graphene (0.3 eV).^{33–37} Besides, rich terminal groups on the surface of $\text{Ti}_3\text{C}_2\text{T}_x$ are more favorable for interfacial assembly with other species. Moreover, owing to the abundant surface redox reactions, $\text{Ti}_3\text{C}_2\text{T}_x$ also displays significant pseudocapacitive contribution rather than only works as conductive matrix.^{38–41}

Some efforts on Si/MXene composites have been made, where Si nanoparticles randomly sandwiched between MXene nanosheets were prepared by physically mixing the two components^{42–45} or *in situ* magnesiothermic/aluminothermic reductions from MXene nanosheets/ SiO_2 composites.^{46,47} It is noteworthy that Si nanoparticles sandwiched between MXene sheets are in a loose contact manner with limited contact interface between Si and MXene, which may lead to an ineffective interfacial electron transfer and easily falling off of Si components from electrode to electrolyte solution during cycling.

In this work, a core–shell architected composite where $\text{Ti}_3\text{C}_2\text{T}_x$ nanosheets (TNSs) as a conductive and robust tight were closely wrapped on the surface of silicon porous nanospheres (Si p-NSs) has been constructed as the stable and high-capacity anode for high-performance LIBs. The Si p-NS@TNSs composite was realized through the separate preparation of the Si p-NSs by a magnesiothermic reduction and $\text{Ti}_3\text{C}_2\text{T}_x$ nanosheets by chemical etching, followed via an interfacial assembly process. There is a set of advantages of the Si p-NS@TNSs composite as LIBs anodes. First, the close wrapping of TNSs around Si p-NSs can not only protect the Si p-NSs from directly contacting with the electrolyte but also provide large contacting interface between the two components for efficient interfacial electron transfer; second, TNSs as a robust and conductive tight with excellent flexibility are helpful to enhance the electrical conductivity of the Si p-NSs and simultaneously accommodate their expansion strain to avoid being pulverized based on experiment measurements and mechanical simulations; last but not least, XPS results evidence that there exists the strong Si–O–Ti interaction at the Si– $\text{Ti}_3\text{C}_2\text{T}_x$ interface, which is beneficial for reinforced interfacial electron transport and enhanced cycling stability. As a result, the Si p-NS@TNSs electrode exhibits significantly enhanced performance in half cells or full cells of LIBs compared with the bare Si electrode.

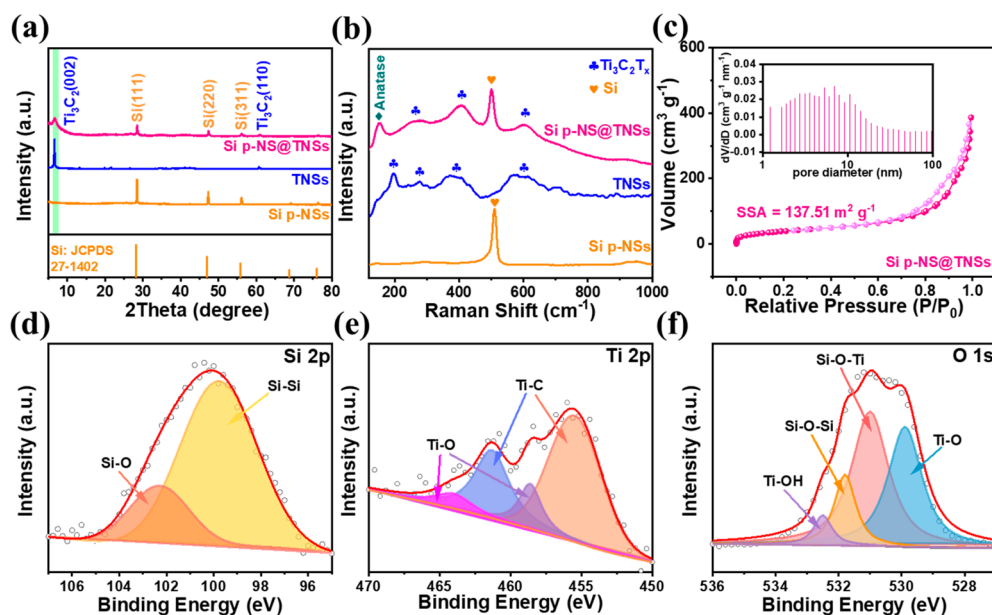


Figure 2. (a) XRD patterns and (b) Raman spectra of the Si p-NS@TNSs composite, TNSs, and Si p-NSs. (c) Nitrogen adsorption–desorption isotherm of the Si p-NS@TNSs composite. Inset in panel c shows the BJH pore size distribution of the Si p-NS@TNSs composite. (d–f) High-resolution XPS spectra of (d) Si 2p, (e) Ti 2p, and (f) O 1s of the Si p-NS@TNSs composite.

RESULTS AND DISCUSSION

The synthetic process for the Si p-NS@TNSs composite is schematically demonstrated in Figure 1a, which includes the preparation of TNSs and Si p-NSs separately and the subsequent interfacial assembly of the two components. Briefly, TNSs, with single or few-layer thinness and diameters ranging from several hundred nanometers to micrometers (Figure S1), were made by chemical etching of Ti_3AlC_2 precursor followed by sonication treatment,⁴⁸ while Si p-NSs were obtained from SiO_2 nanospheres (Figure S2) via a magnesiothermic reduction,^{49,50} accompanied by the conversion of SiO_2 solid nanospheres to Si porous nanospheres (Figures S3 and S4). Prior to the interfacial assembly, the as-synthesized Si p-NSs were first modified with 3-methacryloxypropyltrimethoxysilane (MPS) and then coated with poly(methyl methacrylate) (PMMA) by *in situ* emulsion polymerization (Figure S5). Because of the strong interfacial interaction between TNSs and PMMA,^{51,52} the modified Si p-NSs can be spontaneously wrapped by the TNSs, exhibiting a core–shell structure. Finally, the Si p-NS@TNSs composite was obtained after removing the PMMA via thermal treatment at 500 °C in inert gas atmosphere.

Figure 1b shows the scanning electron microscopy (SEM) image of the modified Si p-NSs coated with PMMA layer. It is found that the thin PMMA layer for interfacial assembly uniformly covers on the surface of silicon porous nanospheres, which is also observed by the corresponding transmission electron microscopy (TEM) image (inset in Figure 1b). For the Si p-NS@TNSs composite, it can be seen that each Si p-NS is closely wrapped by a thin layer of flexible TNSs, forming a core–shell structured composite with a wrinkled surface (Figure 1c). The TNSs shells of the composite are interconnected to form a conductive network. The core–shell structure of the Si p-NS@TNSs composite is further confirmed by the TEM image in Figure 1d, where the porous spherical core (~500 nm in diameter) and ultrathin crumpled shell (~5 nm in thickness) are clearly observed. A high-

resolution transmission electron microscope (HRTEM) image (Figure 1e) presents a lattice spacing of 0.31 nm and an interlayer spacing of 1.31 nm, corresponding to the (111) plane of Si crystal (JCPDS 27–1402) and the (002) plane of $\text{Ti}_3\text{C}_2\text{T}_x$, respectively. Furthermore, the scanning transmission electron microscope (STEM) image of the Si p-NS@TNSs composite and the corresponding energy dispersive spectrum (EDS) mapping images are further illustrated in Figure 1f, indicating the presence and uniform distribution of Si, Ti, and C elements. Through the element distribution images, it is obvious that the Si p-NS is evenly and tightly wrapped by TNSs, indicating the successful preparation of the core–shell structured composite.

Figure 2a shows the X-ray diffraction (XRD) patterns of the Si p-NSs, TNSs, and the Si p-NS@TNSs composite. Three strong diffraction peaks at 28.4°, 47.3°, and 56.1° in the XRD pattern of the Si p-NSs are assigned to the (111), (220), and (311) planes of cubic Si crystal (JCPDS 27–1402), respectively. The XRD pattern of the TNSs shows an intensified peak at 6.6° corresponding to the ~1.33 nm interlayer spacing of characteristic (002) diffraction, which is in accordance with the TEM data and previous literature.⁵³ As for the Si p-NS@TNSs sample, there are two sets of peaks derived from the (111), (220), and (311) planes of the Si p-NSs and the (002) and (110) planes of the TNSs, respectively. It is noted that the main peak of the TNSs in the composite becomes much weaker and broader compared to their pristine counterpart, which may be due to the interlayer distance change of nanosheets caused by the bending of the TNSs on the Si p-NSs. Raman spectra of the three samples are shown in Figure 2b. It is found that the peaks of the Si p-NS@TNSs composite are derived from the two components of the Si and TNSs, except for one near 149 cm^{-1} belonging to anatase^{52,54} caused possibly by slight oxidation of the TNSs during heating treatment. The Raman result is in good agreement with the XRD characterization. Furthermore, the nitrogen adsorption–desorption isotherm of the Si p-NS@TNSs was studied to characterize its surface area and pore size parameters. As

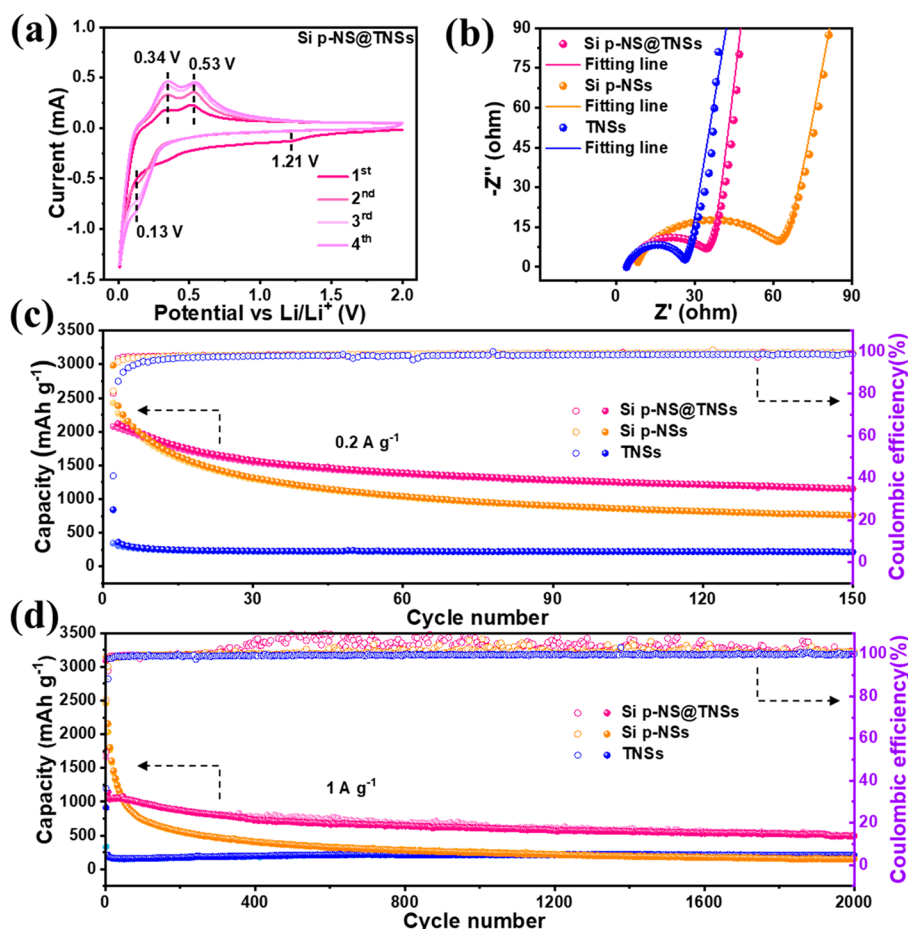


Figure 3. (a) CV curves of the Si p-NS@TNSs composite at a scan rate of 0.1 mV s^{-1} . (b) EIS of the Si p-NS@TNSs, Si p-NSs, and TNSs electrodes. (c) Cycling performance of the Si p-NS@TNSs, Si p-NSs, and TNSs electrodes at 0.2 A g^{-1} . (d) Long cycle performance of the Si p-NS@TNSs, Si p-NSs, and TNSs electrodes at 1 A g^{-1} for 2000 cycles.

shown in Figure 2c, the Brunauer–Emmett–Teller (BET) surface area of the Si p-NS@TNSs was measured to be $137.51 \text{ m}^2 \text{ g}^{-1}$ (Table S1), which is similar to the BET surface area of the Si p-NSs ($124.91 \text{ m}^2 \text{ g}^{-1}$), but much larger than that of the SiO_2 precursor ($8.92 \text{ m}^2 \text{ g}^{-1}$, Figure S6). A typical type-IV isotherm with a type H3 hysteresis loop is observed in the adsorption–desorption curve, revealing the disordered mesoporous structure of the composite. Besides, the Barrett–Joyner–Halenda (BJH) pore size distribution curve of the Si p-NS@TNSs composite shows that there mainly exist mesopores and micropores in the range of about 1–20 nm originated from the stack of the TNSs and Si porous nanospheres.

The interfacial interaction between the Si p-NSs and TNSs in the composite was further investigated by X-ray photoelectron spectroscopy (XPS). A typical XPS survey spectrum of the Si p-NS@TNSs composite in Figure S7 confirms the presence of Si, Ti, and C elements generated from the Si nanospheres and TNSs, in addition to O and F elements from surface terminations of the TNSs. According to high-resolution Si 2p and Ti 2p spectra in Figure 2d and e, Si–O bond at 102.3 eV and Ti–O bond at 464.3 and 458.6 eV are observed, in addition to the typical Si–Si bond at 99.8 eV from the Si p-NSs⁵⁵ and Ti–C bond at 455.6 and 461.4 eV from the TNSs, implying the possible Si–O–Ti interaction at the interface between the Si p-NSs and TNSs.^{38,56} Particularly, the high-resolution O 1s spectrum in Figure 2f displays different peaks

at 532.5, 531.8, 531.0, and 529.9 eV, which can be assigned to Ti–OH, Si–O–Si, Si–O–Ti, and Ti–O bonds, respectively.⁴⁷ The existence of the strong Si–O–Ti interfacial interaction can facilitate interfacial electron transfer and reinforce structure stability of the composite, which is beneficial for battery performance improvement.

The electrochemical performance of the Si p-NS@TNSs composite with a Si content of 85.6% was investigated as well as the Si p-NSs and TNSs for comparison. Cyclic voltammetry (CV) measurements were performed to investigate the lithiation and delithiation reactions of the three samples. Figure 3a exhibits the first four CV curves of the Si p-NS@TNSs electrode between 0.01 and 2 V (vs Li/Li^+) at a sweep rate of 0.1 mV s^{-1} . For a comparison, the Si p-NSs and TNSs electrodes are also examined under the same condition (Figure S8). In the first cycle, a broad reduction peak appears at 1.21 V and disappears in subsequent cycles, which is ascribed to the irreversible reaction between electrolyte and surface functional group of TNSs and the formation of a stable solid electrolyte interphase (SEI) film.⁴⁵ In the subsequent cycles, a cathodic peak at $\sim 0.13 \text{ V}$ appears, related to the lithiation of Si to form Li_xSi ($0 \leq x \leq 4.4$). In the anodic scans, two oxidation peaks at ~ 0.34 and 0.53 V are observed, attributing to the delithiation of Li_xSi to form Si, which is similar to the CV of the Si p-NSs (Figure S8a).⁵⁰ The electrochemical impedance spectroscopy (EIS) measurements were applied to the three electrodes to explore their electronic/ionic transport behaviors. As shown in

Figures 3b and S9, the calculated contact resistance (R_c) and charge transfer resistance (R_{ct}) for the Si p-NS@TNSs electrode are 4.13 and 32.67 Ω (Table S2), respectively. The values are a little larger than those of the TNSs ($R_s = 3.94 \Omega$ and $R_{ct} = 21.93 \Omega$) but much smaller than the pristine Si p-NSs ($R_s = 6.98 \Omega$, $R_{ct} = 58.30 \Omega$). The result demonstrates that the Si p-NS@TNSs electrode displays a lower charge transfer impedance and faster electron transport as well as excellent reversibility after wrapping of the TNSs.

The representative galvanostatic charge/discharge profiles of the Si p-NS@TNSs electrode in the first, second, 50th, 100th, and 150th cycle at 0.2 A g⁻¹ display a discharge plateau between 0.2 and 0.05 V and a charge plateau between 0.3 and 0.5 V (Figure S10a), which are in good accordance with the CV results. It is noted that all electrochemical data are calculated based on the overall mass of the Si and TNSs. The capacity of the first discharge and charge is 2588 and 2077 mAh g⁻¹, respectively, corresponding to an initial Coulombic efficiency (ICE) of 80.2%. Meanwhile, the coulomb efficiency reaches 96.8% in the second cycle. The cycling performance tests are shown in Figure 3c. The Si p-NS@TNSs electrode delivers a high reversible specific capacity of 1154 mAh g⁻¹ after 150 cycles at a current density of 0.2 A g⁻¹, which is much larger than those of the Si p-NSs (760 mAh g⁻¹) and TNSs (215 mAh g⁻¹) electrodes. The long-term cycling test of the three electrodes at a current density of 1A g⁻¹ was also performed, as shown in Figure 3d. Prior to the test, a low current density of 0.1 A g⁻¹ was applied to the three electrodes for initial five cycles, followed by using 1 A g⁻¹ in subsequent cycles. According to Figure 3d, the Si p-NS@TNSs electrode maintains a capacity of 501 mAh g⁻¹ after 2000 cycles, with a low capacity decay rate of 0.026% per cycle, demonstrating outstanding cycling stability. In contrast, the Si p-NSs electrode shows an obvious capacity attenuation, retaining only 153 mAh g⁻¹ after 2000 cycles. The TNSs electrode, though stable, delivers a low capacity of 206 mAh g⁻¹ due to the pseudocapacitive energy storage behavior. In addition, the Si p-NS@TNSs electrode also exhibits good rate capability at various current densities increased dramatically from the initial 0.1 A g⁻¹ to 4 A g⁻¹. The reversible capacities of 1498, 1331, 1248, 1161, 1054, and 899 mAh g⁻¹ for the Si p-NS@TNSs electrode are obtained at 0.1, 0.2, 0.5, 1, 2, and 4 A g⁻¹, respectively (Figures S10b,c, Table S3). It should be emphasized that after switching the current density back to the previous 0.5 A g⁻¹, the capacity is recovered to 1132 mAh g⁻¹, giving a 90.7% capacity retention. In contrast, the TNSs electrode exhibits much lower capacity than the Si p-NS@TNSs electrode at each rate, and the Si p-NSs electrode shows rapidly capacity fading with increasing current density. Notably, the Si p-NS@TNSs electrode still keeps the electrode integrity after 500 cycles at 1 A g⁻¹ with a much smaller electrode thickness change ratio (12.5%) than the electrode based on the Si p-NSs (136.7%) (Figure S11). In addition, as shown in Figure S12, the core-shell morphology of the Si p-NS@TNSs composite can be well preserved after high-rate and long-term cycling, but the structure of the Si p-NSs is severely shattered.

Furthermore, other Si p-NS@TNSs samples with different Si contents (90.5%, 66.2%) were synthesized by controlling the feed ratio of Si and TNSs and measured by inductive coupled plasma emission spectrometer (ICP-MS) to compare their battery performance with the typical Si p-NS@TNSs composite (Si content: 85.6%) (Figures S13 and S14). It is

clear that the sample with a high Si content of 90.5% delivers the highest initial specific capacity but the poorest cycle stability, due to the insufficient wrapping of TNSs, which may cause poor electrical conductivity and easy pulverization/collapse of Si anode. It is also found that the sample with a low Si content (66.2%) has the lowest capacity during the whole cycling process due to the least Si content plus too thick wrapping of TNSs that may impede lithium-ion diffusion across the TNS shells to the Si cores (Figure S14). It is noted that a different synthetic route to TNSs-wrapped Si p-NSs was also conducted, which includes directly wrapping of TNSs on the surface of SiO₂ nanospheres, followed by the same magnesiothermic reduction at 700 °C (Figure S15). However, it was found that SiC phase was unavoidably produced during the reduction and existed in the final product, accompanied by the damage of the TNSs chemically, resulting in serious deterioration of battery performance (Figures S16 and S17). Therefore, for our proposed strategy, the separate magnesiothermic reduction of SiO₂ for Si preparation, which avoids SiC generation, is essential for achieving the Si p-NS@TNSs composite and excellent battery performance. Furthermore, we prepared a control sample of directly mixing MXene and Si p-NSs (Si p-NS/TNSs). As shown in Figure S18, there are many exposed silicon surfaces of Si p-NSs. The Si p-NS/TNSs electrode shows an obvious capacity attenuation, which is much worse than the Si p-NS@TNSs (Figure S19). In addition, a full cell based on the Si p-NSs anode and commercial cathode (LiFePO₄) can uptake gravimetric energy densities of 385 Wh kg⁻¹ in the initial and 405 Wh kg⁻¹ in the 80th cycle, much higher than that of the full cell based on the Si p-NS@TNSs anode as well as the presently commercial LIBs (Figures S20 and S21).⁵⁷

It is well-known that Si is a representative LIB anode associating with alloying reactions,⁵⁸ while Ti₃C₂T_x MXene is recognized as a kind of pseudocapacitive materials due to its surface redox reactions. Hence, the Si p-NS@TNSs electrode integrating Si and Ti₃C₂T_x involves a so-called battery-capacitive dual-model energy storage (DMES) behavior.⁵⁸ To gain further insight into the battery-capacitive DMES mechanism, electrochemistry kinetics analyses based on CV were carried out. As shown in Figure 4a, CV curves are obtained at different scan rates (0.2–2 mV s⁻¹), showing similar shapes with broad peaks. Here the judgment of capacitance behavior can be analyzed based on the relationship between the measured current (I) and the scan rate (ν) in the formula below:⁵⁹

$$I = a\nu^b \quad (1)$$

Both a and b are adjustable values; b can be derived from the slope of the $\log(\nu) - \log(i)$ plots. Generally, $b = 0.5$ implies a diffusion-controlled behavior, while $b = 1$ relates to a capacitive process free of diffusion limitations. A b value of 0.64 can be obtained in Figure 4b, indicating that the battery-capacitive DMES mechanism is involved in the Si p-NS@TNSs electrode. For the TNSs electrode, the b value is calculated to be 0.91 (Figure S22a,b), which is much higher than that of the Si p-NS@TNSs electrode. This indicates that the capacitive contribution of the Si p-NS@TNSs electrode is mainly provided by the TNS component. Also, the capacitive contribution ratio between the two different processes at a specific scan rate can be calculated quantitatively according to the equation:

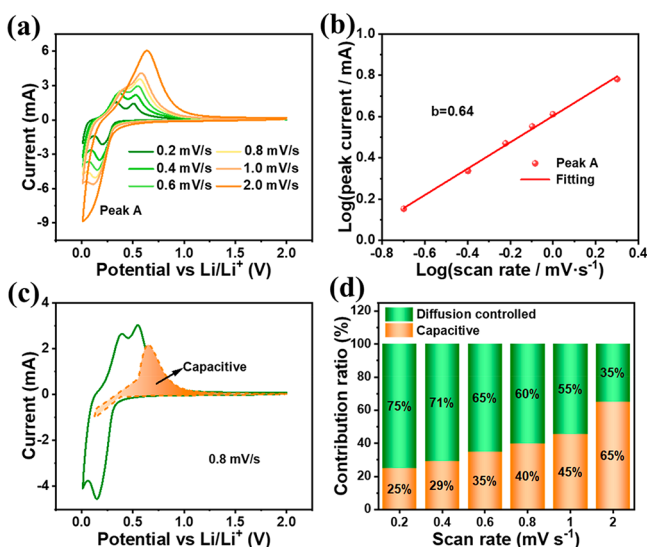


Figure 4. (a) CV curves of the Si p-NS@TNSs electrode at various scan rates from 0.2 to 2 mV s⁻¹. (b) Relationship between the log(peak current) and log(scan rate). (c) Contribution of capacitive charge storage to the total capacity of the Si p-NS@TNSs composite electrode at a scan rate of 0.8 mV s⁻¹. (d) Contribution ratio of the capacitive and diffusion-controlled charge storage at different scan rates.

$$i(v) = k_1v + k_2v^{1/2} \quad (2)$$

where $i(v)$, k_1v , $k_2v^{1/2}$, and v are the current at a given voltage, capacitive current, diffusion-controlled current, and scan rate, respectively.⁶⁰ On the basis of the integral calculation, 40% of the total Li⁺ storage capacity in the Si p-NS@TNSs electrode comes from the capacitive process at a scan rate of 0.8 mV s⁻¹ (Figure 4c,d), which is lower than that of the TNSs (81%) (Figure S22c,d). In the light of the capacitive contribution ratios at different scan rates in Figure 4d, it is clearly that as the scanning speed increases, the pseudocapacitive effect of the composite material is gradually enhanced, reaching 65% at 2 mV s⁻¹. These results suggest that the energy storage process of the Si p-NS@TNSs anode is in accordance with the battery-capacitive DMES mechanism, which is beneficial to fast charging and long-cycling stability.

To deeply understand the origin of structural stability of the Si p-NS@TNSs electrode during the lithiation process, a simulation of elastic–plastic evolution coupled to Li diffusion of both the Si p-NS@TNSs and Si p-NSs electrodes was adopted. Figure 5 shows the simulated results for the Si p-NS@TNSs composite and the Si p-NSs. The employed configurations of the Si p-NS@TNSs composite and the Si p-NSs for simulations and stress evolution during lithiation process are shown in Figure 5a. The yellow circular inside represents the Si p-NS and the outer dark blue ring stands for TNS shell. Considering the porous characteristic of the Si p-NSs, a parameter was introduced to reflect the porosity of the Si p-NSs and was defined as P . Accordingly, the Young's modulus of the Si p-NSs can be estimated by $Y = A(1 - P)^3$,⁶¹ where A is a constant. It should be noted that our diffusion simulations mainly focus on the stress generated in the Si structure rather than the protective shell of the TNSs. Upon charging, stresses occurred inside the composites as the Li ion diffused (Figure S23). The radial and hoop stress distribution during the lithium process is displayed in Figure 5b and c.

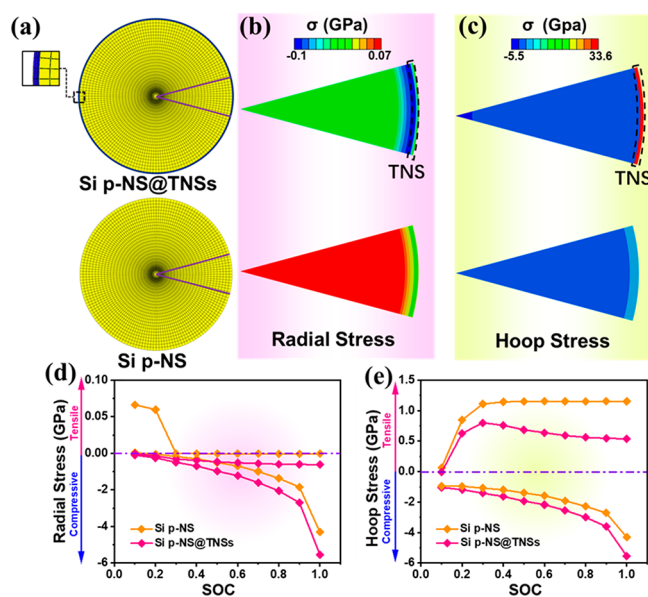


Figure 5. (a) Finite element simulations models of the Si p-NS@TNSs composite and the Si p-NS. (b, c) Radial and hoop stress distributions of 30° sector area of the Si p-NS@TNSs composite and the Si p-NS during lithiation process. (d, e) Evolution of (d) radial stress and (e) hoop stress in the Si p-NS@TNSs composite and the Si p-NS at different state of charge (SOC).

Different colored areas from red to blue signify different tensile stress states (represented by positive values) and compressive stress states (represented by negative values). While radial stress occurred during the lithiation process, the Si p-NS@TNSs sample was mainly suffered compressive radial stress, which was different from the tensile radial stress at the beginning of the Si p-NSs. It was found that the regions of the shell of the Si p-NS@TNSs are red with high hoop stress. However, the stress at the interface between the Si p-NS and TNSs drops off sharply due to the constraint of the outer shell, thus avoiding the electrode fracture. Figure 5d and e draw the evolution of maximum and minimum radial and hoop stress when the state of charge (SOC) value ranges from 0 to 1 by analyzing original data from the Figure S24. In the simulation, we pay more attention to tensile stress because it is the key factor in the collapse of the electrode structure. It is clear that the tensile stress of the Si p-NS@TNSs composite is always lower than the Si p-NS in both radial and hoop stress. In addition, the Si p-NS@TNSs composite undergoes a maximum hoop tensile stress of 0.8 GPa at SOC = 0.3, which is much lower than that of the Si p-NS (1.15 GPa) (Figure 5e). Moreover, compressive stress filled in most area of the Si p-NS@TNSs and inhibits the initiation and propagation of cracks. To sum up, the TNS shells can effectively reduce surface tension during lithiation of Si, which is helpful to enhance the structural stability for long-term cycling.

CONCLUSION

In conclusion, the core–shell composite of the Si p-NS@TNSs where Si p-NSs are tightly wrapped by TNSs has been fabricated through an interfacial assembly coupling with magnesiothermic reductions. The TNSs as conductive and robust tight plus strong interfacial interaction with Si component endow the composite with enhanced electrical conductivity and high structure stability against pulverization,

responsible for comprehensive performance improvement of lithium storage. In addition, the mechanical simulations also quantitatively reveal both lower radial and hoop stress generated for the Si p-NS@TNSs composite anode upon lithiation, confirming that the wrapping of TNSs is effective to reinforce the structure stability of Si anodes. The core-shell architecture of the Si p-NS@TNSs may present as a typical mechanics model for designing highly stable electrodes. This study provides a strategy to develop excellent electrode materials using MXene as functional tightts for energy applications.

EXPERIMENTAL SECTION

Synthesis of $Ti_3C_2T_x$. A 0.5 g sample of Ti_3AlC_2 powders (Carbon-Ukraine, Ltd) was slowly added to a mixture of 0.5 g of lithium fluoride (LiF) and 10 mL of 9 M hydrochloric acid (HCl) under stirring at 40 °C for 24 h to exfoliate the Al layers. Then the obtained product was washed by deionized water and centrifuged several times until the pH of the supernatant reached 6. Finally, the sample was dried in vacuum at 60 °C for 8 h.

Preparation of TNSs. In a typical procedure, 100 mg of the as-prepared $Ti_3C_2T_x$ powders was dispersed in 20 mL of oxygen-free deionized water (DI water) by passing Argon gas. The suspension was ultrasound for 1 h and was centrifuged at 3500 rpm for 1 h. After that, black precipitate and dark green supernatant were obtained. The supernatant was collected for further use.

Preparation of SiO_2 NSs. The modified Stöber process was used to synthesize SiO_2 nanospheres. Specifically, ethanol (16.25 mL), NH_3H_2O (32 wt %, 9 mL), and DI water (24.75 mL) were mixed under intense stirring for 15 min, followed by the dropwise adding of the mixed solution of tetraethyl orthosilicate (TEOS, 4.5 mL) and DI water (45.5 mL), and further stirring at room temperature for 2 h. After the reaction, the final products were washed using water and ethanol repeatedly and collected by centrifuging and vacuum drying.

Preparation of Si p-NSs. Typically, the prepared silica was mixed with Mg powder (powder, 99%, Aldrich) at a weight ratio of 1:1 and added into a stainless-steel autoclave. The autoclave was heated at 700 °C for 6 h under argon atmosphere with a heating rate of 1 °C min^{-1} . After cooling down to room temperature, the resulting powder was dispersed in a 1 M HCl solution for 5 h to remove MgO and the remaining Mg. To remove unreacted silica and MgSi, the powder was immersed in ethanol-based hydrofluoric acid (HF, 5%) solution for 30 min, followed by washing with ethanol and DI water and drying at 80 °C overnight. The obtained Si showed mesoporous structure after magnesiothermic reduction.

Preparation of Si p-NS@TNSs Composite. First, Si p-NSs were first modified with methacryloxy propyl trimethoxyl silane (MPS) molecules. Specifically, 120 mg of Si p-NSs was dispersed in the mixture solution of 80 mL of ethanol, 0.2 mL of NH_3H_2O , 1.2 mL of MPS, and 2 mL of H_2O at room temperature and stirred for 2 days. Second, the Si p-NS@PMMA spheres were obtained by polymerization of the methyl methacrylate (MMA). To be specific, 50 mg of MPS modified Si p-NSs, 10 mg of sodium dodecyl sulfate (SDS), 0.8 g of polyvinylpyrrolidone (PVP), and 120 mL of DI water are premixed in a three-neck flask under room temperature while stirring overnight to form a uniform mixture suspension A. After the temperature reached to 60 °C, 2 mL of potassium persulfate (KPS) solution (20 mg mL^{-1}) was added in the flask under the protection of nitrogen. Next, emulsion B made of 20 mg of SDS, 20 mL of H_2O , 4 mL of MMA, and 30 mg of KOH was slowly dropped into the flask in 15 min, followed by raising the temperature to 70 °C. After polymerization at 70 °C under Ar for 1 h, the Si p-NS@PMMA colloids were collected and washed with water by centrifugation. The sample was then dispersed in water by sonication for 30 min. Third, the TNS colloidal solution (2 mg mL^{-1}) and the Si p-NS@PMMA dispersion (3 mg mL^{-1}) were directly mixed together and kept under stirring for 10 min. The mixture was centrifuged at 6000 r/ppm and then collected and dried at 80 °C. Finally, the Si p-NS@TNS product

was obtained after PMMA was removed by annealing at 500 °C for 2 h under flowing Ar gas. As a comparison, the contents of Si in the resulting composite could be easily adjusted by controlling the feeding ratio of the Si p-NSs and TNSs.

Characterizations. The morphologies and microstructures were characterized by a scanning electron microscopy (SEM, Hitachi S-4800, 3 kV) and a high-resolution transmission electron microscope (HRTEM, JEOL JEM2100F, 24 200 kV) together with associated energy-dispersive X-ray spectroscopy (EDS). X-ray diffraction patterns (XRD) were obtained by using a D8 advance X-ray diffractometer with a Cu $K\alpha$ radiation source ($\lambda = 0.15418$ nm) in a step of 0.02° over a 2θ range of 5–80°. Raman spectra were performed on a Laser Raman spectrometer (in Via, Renishaw, Germany) with a 514 nm laser. The Raman band of a silicon wafer at 520 cm^{-1} was used as a reference to calibrate the spectrometer. The surface area was measured from the N_2 adsorption and desorption isotherms by the Brunauer–Emmett–Teller (BET) method. The pore size distributions were retrieved by using the Barrett–Joyner–Halanda (BJH) method from the adsorption branch of the isotherms. An X-ray photoelectron spectroscopy (XPS) PHI-5000C ESCA system (PerkinElmer) with Mg $K\alpha$ radiation and the C 1s peak at 284.6 eV as internal standard was used to analyze the surface elemental composition of the powders. The content of Si, Ti element in the composite was determined with an inductive coupled plasma emission spectrometer (ICP-MS) (PerkinElmer Optima 8000).

Electrochemical Measurements. The working electrode was prepared by casting slurries consisting of the active materials, acetylene black (Super-P), and 10% PVDF at a weight ratio of 7:2:1 onto pure copper foil collector. After casting, the electrodes were dried at 80 °C for 12 h in a vacuum oven. The mass loading of active materials in the electrodes was about 1.0 mg cm^{-2} . Then the prepared working electrodes were assembled into 2016-type coin half cells (MTI Corporation) in an argon-filled glovebox (Mikrouna Super 2440/750/900) with the levels of oxygen and moisture below 0.1 ppm. The electrolyte was 1.0 M LiPF₆ with a mixture of ethylene carbonate (EC), dimethyl carbonate (DMC), and ethyl methyl carbonate (EMC) (1:1:1 in volume). Glass fibers (GF/D) from Whatman were used as separators, and pure lithium metal foil was used as the negative electrode.

The rate performance tests and galvanostatic charging/discharging (GCD) measurements were performed on a LAND CT2001A instrument (Wuhan, China) in the voltage range of 0.01–2 V (vs. Li/Li⁺). Cyclic voltammetry (CV) and spectroscopy (EIS) were conducted on CHI660E electrochemical workstation (CH Instruments, Inc., Shanghai). For EIS measurements, an AC amplitude of 5 mV was applied to the cells in the range from 100 kHz to 10 mHz. The specific capacity was measured on the basis of the total weight of the Si p-NS@TNS composite.

Full Battery Assembly. For the construction of full cell, the same electrolyte and separator were used. LiFePO₄ mixed with acetylene black and PVDF (80:10:10, in mass) was spread on Al foil and employed as the cathode. The anode materials were first prelithiated in half cells and then taken out for full cell assembly. The full cell was charged/discharged galvanostatically at 0.1 A g^{-1} and cycled in the range of 2.0–4.0 V on LAND galvanostatic charge/discharge instruments. The specific capacity was calculated based on the LiFePO₄ mass because the battery was cathode-limited.

Method and Model of Finite Element Analysis. We numerically implemented the above diffusion and constitutive equations of elastic–plastic deformation model by using the finite element package ABAQUS. The Li and stress–strain fields were incrementally updated using an implicit coupled temperature–displacement procedure in ABAQUS/Standard. To describe the evolution of diffusion and associated stress generation, fully coupled thermal diffusion–stress analysis was performed in direct finite element simulations.

ASSOCIATED CONTENT

Supporting Information

The Supporting Information is available free of charge at <https://pubs.acs.org/doi/10.1021/acsnano.0c01976>.

Additional characterizations including optical photographs, SEM and TEM images, XRD pattern, spectra BET analyses, FTIR and XPS spectra, mechanical simulations and electrochemical data including CV curves, charge–discharge curves and performance comparison of Si p-NS@TNSs with different Si contents, Si/SiC@TNSs, Si p-NS/TNSs composite and full cells (PDF)

AUTHOR INFORMATION

Corresponding Authors

Haijiao Zhang – Institute of Nanochemistry and Nanobiology, Shanghai University, Shanghai 200444, P. R. China; orcid.org/0000-0003-2958-2967; Email: hjzhang128@shu.edu.cn

Chi Zhang – School of Chemical Science and Engineering, Tongji University, Shanghai 200092, P. R. China; Research Center for Translational Medicine & Key Laboratory of Arrhythmias of the Ministry of Education of China, East Hospital, Tongji University School of Medicine, Shanghai 200120, P. R. China; orcid.org/0000-0002-5237-8916; Email: chizhang@tongji.edu.cn

Jinhu Yang – School of Chemical Science and Engineering, Tongji University, Shanghai 200092, P. R. China; Research Center for Translational Medicine & Key Laboratory of Arrhythmias of the Ministry of Education of China, East Hospital, Tongji University School of Medicine, Shanghai 200120, P. R. China; orcid.org/0000-0002-1793-7380; Email: yangjinhu@tongji.edu.cn

Authors

Mengting Xia – School of Chemical Science and Engineering, Tongji University, Shanghai 200092, P. R. China; Research Center for Translational Medicine & Key Laboratory of Arrhythmias of the Ministry of Education of China, East Hospital, Tongji University School of Medicine, Shanghai 200120, P. R. China

Bingjie Chen – School of Chemical Science and Engineering, Tongji University, Shanghai 200092, P. R. China; Research Center for Translational Medicine & Key Laboratory of Arrhythmias of the Ministry of Education of China, East Hospital, Tongji University School of Medicine, Shanghai 200120, P. R. China

Feng Gu – International Research Institute for Minerals, Metallurgy and Materials, Jiangxi University of Science and Technology, Nanchang, Jiangxi 330013, P. R. China

Lianhai Zu – Department of Chemical Engineering, Monash University, Clayton 3800, Australia

Mengzhu Xu – School of Chemical Science and Engineering, Tongji University, Shanghai 200092, P. R. China

Yutong Feng – School of Chemical Science and Engineering, Tongji University, Shanghai 200092, P. R. China

Zhijun Wang – School of Chemistry and Chemical Engineering, Jiangangshan University, Ji'an, Jiangxi 343009, P. R. China

Complete contact information is available at: <https://pubs.acs.org/doi/10.1021/acsnano.0c01976>

Author Contributions

^{||}M.T.X. and B.J.C. contributed equally to this work

Notes

The authors declare no competing financial interest.

ACKNOWLEDGMENTS

This work was financially supported by the National Natural Science Foundation (51972235), the Natural Science Foundation of Shanghai (17ZR1447800), the Program for Professor of Special Appointment (Eastern Scholar) at the Shanghai Institutions of Higher Learning, Shuguang Program supported by Shanghai Education Development Foundation and Shanghai Municipal Education Commission (18SG035), the Hundred Youth Talent Plan of Tongji University, and the Fundamental Research Funds for the Central Universities.

REFERENCES

- (1) Dunn, B.; Kamath, H.; Tarascon, J. Electrical Energy Storage for the Grid: A Battery of Choices. *Science* **2011**, *334*, 928–935.
- (2) Sun, X.; Si, W.; Liu, X.; Deng, J.; Xi, L.; Liu, L.; Yan, C.; Schmidt, O. G. Multifunctional Ni/NiO Hybrid Nanomembranes as Anode Materials for High-Rate Li-Ion Batteries. *Nano Energy* **2014**, *9*, 168–175.
- (3) Scrosati, B.; Hassoun, J.; Sun, Y. Lithium-Ion Batteries. A Look into the Future. *Energy Environ. Sci.* **2011**, *4*, 3287–3295.
- (4) Choi, N.; Chen, D.; Freunberger, D.; Ji, D.; Sun, P.; Amine, P.; Yushin, P.; Nazar, P.; Cho, P.; Bruce, P. Challenges Facing Lithium Batteries and Electrical Double-Layer Capacitors. *Angew. Chem., Int. Ed.* **2012**, *51*, 9994–10024.
- (5) McDowell, M.; Lee, S.; Nix, W.; Cui, Y. 25th Anniversary Article: Understanding the Lithiation of Silicon and Other Alloying Anodes for Lithium-Ion Batteries. *Adv. Mater.* **2013**, *25*, 4966–4985.
- (6) Cui, L.; Ruffo, R.; Chan, C.; Peng, H.; Cui, Y. Crystalline-Amorphous Core-Shell Silicon Nanowires for High Capacity and High Current Battery Electrodes. *Nano Lett.* **2009**, *9*, 491–495.
- (7) Chen, B.; Zu, L.; Liu, Y.; Meng, R.; Feng, Y.; Peng, C.; Zhu, F.; Hao, T.; Ru, J.; Wang, Y.; Yang, J. Space-Confined Atomic Clusters Catalyze Superassembly of Silicon Nanodots within Carbon Frameworks for Use in Lithium-Ion Batteries. *Angew. Chem., Int. Ed.* **2020**, *59*, 3137–3142.
- (8) Liu, Y.; Tai, Z.; Zhou, T.; Sencadas, V.; Zhang, J.; Zhang, L.; Konstantinov, K.; Guo, Z.; Liu, H. An All-Integrated Anode via Interlinked Chemical Bonding between Double-Shelled-Yolk-Structured Silicon and Binder for Lithium-Ion Batteries. *Adv. Mater.* **2017**, *29*, 1703028.
- (9) Nie, P.; Liu, X.; Fu, R.; Wu, Y.; Jiang, J.; Dou, H.; Zhang, X. Mesoporous Silicon Anodes by Using Polybenzimidazole Derived Pyrrolic N-Enriched Carbon toward High-Energy Li-Ion Batteries. *ACS Energy Lett.* **2017**, *2*, 1279–1287.
- (10) Obrovac, M.; Christensen, L. Structural Changes in Silicon Anodes during Lithium Insertion/Extraction. *Electrochem. Solid-State Lett.* **2004**, *7*, A93.
- (11) Luo, W.; Wang, Y.; Wang, L.; Jiang, W.; Chou, S.; Dou, S.; Liu, H.; Yang, J. Silicon/Mesoporous Carbon/Crystalline TiO₂ Nanoparticles for Highly Stable Lithium Storage. *ACS Nano* **2016**, *9*, 10524–10532.
- (12) Casimir, A.; Zhang, H.; Ogoke, O.; Amine, J.; Lu, J.; Wu, G. Silicon-Based Anodes for Lithium-Ion Batteries: Effectiveness of Materials Synthesis and Electrode Preparation. *Nano Energy* **2016**, *27*, 359–376.
- (13) Su, X.; Wu, Q.; Li, J.; Xiao, X.; Lott, A.; Lu, W.; Sheldon, B. W.; Wu, J. Silicon-Based Nanomaterials for Lithium-Ion Batteries: A Review. *Adv. Energy Mater.* **2014**, *4*, 1300882.
- (14) Adkins, E.; Jiang, T.; Luo, L.; Wang, C.; Korgel, B. *In Situ* Transmission Electron Microscopy of Oxide Shell-Induced Pore Formation in (De)lithiated Silicon Nanowires. *ACS Energy Lett.* **2018**, *3*, 2829–2834.

- (15) Feng, K.; Ahn, W.; Lui, G.; Park, H.; Kashkooli, A.; Jiang, G.; Wang, X.; Xiao, X.; Chen, Z. Implementing an *In Situ* Carbon Network in Si/Reduced Graphene Oxide for High Performance Lithium-Ion Battery Anodes. *Nano Energy* **2016**, *19*, 187–197.
- (16) Lee, J.; Smith, K.; Hayner, C.; Kung, H. Silicon Nanoparticles-Graphene Paper Composites for Li Ion Battery Anodes. *Chem. Commun.* **2010**, *46*, 2025–2027.
- (17) Nie, P.; Le, Z.; Chen, G.; Liu, D.; Liu, X.; Wu, H.; Xu, P.; Li, X.; Liu, F.; Chang, L.; Zhang, X.; Lu, Y. Graphene Caging Silicon Particles for High-Performance Lithium-Ion Batteries. *Small* **2018**, *14*, 1800635.
- (18) Ji, J.; Ji, H.; Zhang, L.; Zhao, X.; Bai, X.; Fan, X.; Zhang, F.; Ruoff, R. Graphene-Encapsulated Si on Ultrathin-Graphite Foam as Anode for High Capacity Lithium-Ion Batteries. *Adv. Mater.* **2013**, *25*, 4673–4677.
- (19) Wu, J.; Cao, Y.; Zhao, H.; Mao, J.; Guo, Z. The Critical Role of Carbon in Marrying Silicon and Graphite Anodes for High-Energy Lithium-Ion Batteries. *Carbon Energy* **2019**, *1*, 57–76.
- (20) Agyeman, D.; Song, K.; Lee, G.; Park, M.; Kang, Y. Carbon-Coated Si Nanoparticles Anchored between Reduced Graphene Oxides as an Extremely Reversible Anode Material for High Energy-Density Li-Ion Battery. *Adv. Energy Mater.* **2016**, *6*, 1600904.
- (21) Shan, C.; Wu, K.; Yen, H.; Narvaez Villarrubia, C.; Nakotte, T.; Bo, X.; Zhou, M.; Wu, G.; Wang, H. Graphene Oxides Used as a New “Dual Role” Binder for Stabilizing Silicon Nanoparticles in Lithium-Ion Battery. *ACS Appl. Mater. Interfaces* **2018**, *10*, 15665–15672.
- (22) Peng, C.; Chen, H.; Li, Q.; Cai, W.; Yao, Q.; Wu, Q.; Yang, J.; Yang, Y. Synergistically Reinforced Lithium Storage Performance of *In Situ* Chemically Grown Silicon@Silicon Oxide Core-Shell Nanowires on Three-Dimensional Conductive Graphitic Scaffolds. *J. Mater. Chem. A* **2014**, *2*, 13859–13867.
- (23) Salvatierra, R.; Raji, A.; Lee, S.; Ji, Y.; Li, L.; Tour, J. Silicon Nanowires and Lithium Cobalt Oxide Nanowires in Graphene Nanoribbon Papers for Full Lithium Ion Battery. *Adv. Energy Mater.* **2016**, *6*, 1600918.
- (24) Chen, J.; Bie, L.; Sun, J.; Xu, F. Enhanced Electrochemical Performances of Silicon Nanotube Bundles. *Mater. Res. Bull.* **2016**, *73*, 394–400.
- (25) Liu, X.; Zhang, J.; Si, W.; Xi, L.; Eichler, B.; Yan, C.; Schmidt, O. Sandwich Nanoarchitecture of Si-Reduced Graphene Oxide Bilayer Nanomembranes for Li-Ion Batteries with Long Cycle Life. *ACS Nano* **2015**, *9*, 1198–1205.
- (26) Wu, P.; Wang, H.; Tang, Y.; Zhou, Y.; Lu, T. Three-Dimensional Interconnected Network of Graphene-Wrapped Porous Silicon Spheres: *In Situ* Magnesium-Thermic-Reduction Synthesis and Enhanced Lithium-Storage Capabilities. *ACS Appl. Mater. Interfaces* **2014**, *6*, 3546–3552.
- (27) Naguib, M.; Kurtoglu, M.; Presser, V.; Lu, J.; Niu, J.; Heon, M.; Hultman, L.; Gogotsi, Y.; Barsoum, M. Two-Dimensional Nanocrystals: Two-Dimensional Nanocrystals Produced by Exfoliation of Ti_3AlC_2 . *Adv. Mater.* **2011**, *23*, 4248–4253.
- (28) Naguib, M.; Mochalin, V.; Barsoum, M.; Gogotsi, Y. 25th Anniversary Article: MXenes: A New Family of Two-Dimensional Materials. *Adv. Mater.* **2014**, *26*, 992–1005.
- (29) Yu, L.; Hu, L.; Anasori, B.; Liu, Y.; Zhu, Q.; Zhang, P.; Gogotsi, Y.; Xu, B. MXene-Bonded Activated Carbon as a Flexible Electrode for High-Performance Supercapacitors. *ACS Energy Lett.* **2018**, *3*, 1597–1603.
- (30) Shi, Y.; Li, B.; Zhu, Q.; Shen, K.; Tang, W.; Xiang, Q.; Chen, W.; Liu, C.; Luo, J.; Yang, S. MXene-Based Mesoporous Nanosheets toward Superior Lithium Ion Conductors. *Adv. Energy Mater.* **2020**, *10*, 1903534.
- (31) Liu, L.; Chen, W.; Zhang, H.; Wang, Q.; Guan, F.; Yu, Z. Flexible and Multifunctional Silk Textiles with Biomimetic Leaf-Like MXene/Silver Nanowire Nanostructures for Electromagnetic Interference Shielding, Humidity Monitoring, and Self-Derived Hydrophobicity. *Adv. Funct. Mater.* **2019**, *29*, 1905197.
- (32) Tang, H.; Li, W.; Pan, L.; Tu, K.; Du, F.; Qiu, T.; Yang, J.; Cullen, C.; McEvoy, N.; Zhang, C. A Robust, Freestanding MXene-Sulfur Conductive Paper for Long-Lifetime Li-S Batteries. *Adv. Funct. Mater.* **2019**, *29*, 1901907–1901917.
- (33) Kong, F.; He, X.; Liu, Q.; Qi, X.; Zheng, Y.; Wang, R.; Bai, Y. Effect of Ti_3AlC_2 Precursor on the Electrochemical Properties of the Resulting MXene Ti_3C_2 for Li-Ion Batteries. *Ceram. Int.* **2018**, *44*, 11591–11596.
- (34) Er, D.; Li, J.; Naguib, M.; Gogotsi, Y.; Shenoy, V. Ti_3C_2 MXene as a High Capacity Electrode Material for Metal (Li, Na, K, Ca) Ion Batteries. *ACS Appl. Mater. Interfaces* **2014**, *6*, 11173–11179.
- (35) Tang, Q.; Zhou, Z.; Shen, P. Are MXenes Promising Anode Materials for Li Ion Batteries? Computational Studies on Electronic Properties and Li Storage Capability of Ti_3C_2 and $\text{Ti}_3\text{C}_2\text{X}_2$ (X = F, OH) Monolayer. *J. Am. Chem. Soc.* **2012**, *134*, 16909–16916.
- (36) Liu, Y.; Zhang, P.; Sun, N.; Anasori, B.; Zhu, Q.; Liu, H.; Gogotsi, Y.; Xu, B. Self-Assembly of Transition Metal Oxide Nanostructures on MXene Nanosheets for Fast and Stable Lithium Storage. *Adv. Mater.* **2018**, *30*, 1707334.
- (37) Zhang, C.; Cui, L.; Abdolhosseinzadeh, S.; Heier, J. Two-Dimensional MXenes for Lithium-Sulfur Batteries. *InfoMat* **2020**, *1*–26.
- (38) Meng, R.; Huang, J.; Feng, Y.; Zu, L.; Peng, C.; Zheng, L.; Zheng, L.; Chen, Z.; Liu, G.; Chen, B.; Mi, Y.; Yang, J. Black Phosphorus Quantum Dot/ Ti_3C_2 MXene Nanosheet Composites for Efficient Electrochemical Lithium/Sodium-Ion Storage. *Adv. Energy Mater.* **2018**, *8*, 1801514.
- (39) Guo, X.; Zhang, J.; Song, J.; Wu, W.; Liu, H.; Wang, G. MXene Encapsulated Titanium Oxide Nanospheres for Ultra-Stable and Fast Sodium Storage. *Energy Storage Mater.* **2018**, *14*, 306–313.
- (40) Li, J.; Yuan, X.; Lin, C.; Yang, Y.; Xu, L.; Du, X.; Xie, J.; Lin, J.; Sun, J. Achieving High Pseudocapacitance of 2D Titanium Carbide (MXene) by Cation Intercalation and Surface Modification. *Adv. Energy Mater.* **2017**, *7*, 1602725.
- (41) Zhang, C.; Ma, Y.; Zhang, X.; Abdolhosseinzadeh, S.; Sheng, H.; Lan, W.; Pakdel, A.; Heier, J.; Nüesch, F. Two-Dimensional Transition Metal Carbides and Nitrides (MXenes): Synthesis, Properties, and Electrochemical Energy Storage Applications. *Energy Environ. Mater.* **2020**, *0*, 1–27.
- (42) Kong, F.; He, X.; Liu, Q.; Qi, X.; Sun, D.; Zheng, Y.; Wang, R.; Bai, Y. Enhanced Reversible Li-Ion Storage in $\text{Si}@\text{Ti}_3\text{C}_2$ MXene Nanocomposite. *Electrochem. Commun.* **2018**, *97*, 16–21.
- (43) Zhang, C.; Park, S.; Seral-Ascaso, A.; Barwich, S.; McEvoy, N.; Boland, C.; Coleman, J.; Gogotsi, Y.; Nicolosi, V. High Capacity Silicon Anodes Enabled by MXene Viscous Aqueous Ink. *Nat. Commun.* **2019**, *10*, 849.
- (44) Liu, S.; Zhang, X.; Yan, P.; Cheng, R.; Tang, Y.; Cui, M.; Wang, B.; Zhang, L.; Wang, X.; Jiang, Y.; Wang, L.; Yu, H. Dual Bond Enhanced Multidimensional Constructed Composite Silicon Anode for High-Performance Lithium Ion Batteries. *ACS Nano* **2019**, *13*, 8854–8864.
- (45) Tian, Y.; An, Y.; Feng, J. Flexible and Freestanding Silicon/MXene Composite Papers for High-Performance Lithium-Ion Batteries. *ACS Appl. Mater. Interfaces* **2019**, *11*, 10004–10011.
- (46) Zhang, Y.; Mu, Z.; Lai, J.; Chao, Y.; Yang, Y.; Zhou, P.; Li, Y.; Yang, W.; Xia, Z.; Guo, S. MXene-Si@ SiO_x @C Layer-by-Layer Superstructure with Autoadjustable Function for Superior Stable Lithium Storage. *ACS Nano* **2019**, *13*, 2167–2175.
- (47) Hui, X.; Zhao, R.; Zhang, P.; Li, C.; Wang, C.; Yin, L. Low-Temperature Reduction Strategy Synthesized $\text{Si}/\text{Ti}_3\text{C}_2$ MXene Composite Anodes for High-Performance Li-Ion Batteries. *Adv. Energy Mater.* **2019**, *9*, 1901065.
- (48) Alhabeb, M.; Maleski, K.; Anasori, B.; Lelyukh, P.; Clark, L.; Sin, S.; Gogotsi, Y. Guidelines for Synthesis and Processing of Two-Dimensional Titanium Carbide ($\text{Ti}_3\text{C}_2\text{T}_x$ MXene). *Chem. Mater.* **2017**, *29*, 7633–7644.
- (49) Wang, W.; Favors, Z.; Ionescu, R.; Ye, R.; Bay, H.; Ozkan, M.; Ozkan, C. Monodisperse Porous Silicon Spheres as Anode Materials for Lithium Ion Batteries. *Sci. Rep.* **2015**, *5*, 8781.
- (50) Zuo, X.; Xia, Y.; Ji, Q.; Gao, X.; Yin, S.; Wang, M.; Wang, X.; Qiu, B.; Wei, A.; Sun, Z.; Liu, Z.; Zhu, J.; Cheng, Y. J. Self-Templating

Construction of 3D Hierarchical Macro-/Mesoporous Silicon from 0D Silica Nanoparticles. *ACS Nano* **2017**, *11*, 889–899.

(51) Zhao, M.; Xie, X.; Ren, C.; Makaryan, T.; Anasori, B.; Wang, G.; Gogotsi, Y. Hollow MXene Spheres and 3D Macroporous MXene Frameworks for Na-Ion Storage. *Adv. Mater.* **2017**, *29*, 1702410.

(52) Li, X.; Yin, X.; Song, C.; Han, M.; Xu, H.; Duan, W.; Cheng, L.; Zhang, L. Self-Assembly Core-Shell Graphene-Bridged Hollow MXenes Spheres 3D Foam with Ultrahigh Specific EM Absorption Performance. *Adv. Funct. Mater.* **2018**, *28*, 1803938.

(53) Ghidui, M.; Lukatskaya, M.; Zhao, M.; Gogotsi, Y.; Barsoum, M. Conductive Two-Dimensional Titanium Carbide ‘Clay’ with High Volumetric Capacitance. *Nature* **2014**, *516*, 78–81.

(54) Zhang, C.; Pinilla, S.; McEvoy, N.; Cullen, C.; Anasori, B.; Long, E.; Park, S.; Seral-Ascaso, A.; Shmeliov, A.; Krishnan, D.; Morant, C.; Liu, X.; Duesberg, G.; Gogotsi, Y.; Nicolosi, V. Oxidation Stability of Colloidal Two-Dimensional Titanium Carbides (MXenes). *Chem. Mater.* **2017**, *29*, 4848–4856.

(55) Zheng, G.; Xiang, Y.; Xu, L.; Luo, H.; Wang, B.; Liu, Y.; Han, X.; Zhao, W.; Chen, S.; Chen, H.; Zhang, Q.; Zhu, T.; Yang, Y. Controlling Surface Oxides in Si/C Nanocomposite Anodes for High-Performance Li-Ion Batteries. *Adv. Energy Mater.* **2018**, *8*, 1801718.

(56) Halim, J.; Cook, K.; Naguib, M.; Eklund, P.; Gogotsi, Y.; Rosen, J.; Barsoum, M. X-Ray Photoelectron Spectroscopy of Select Multi-Layered Transition Metal Carbides (MXenes). *Appl. Surf. Sci.* **2016**, *362*, 406–417.

(57) Watanabe, S.; Kinoshita, M.; Nakura, K. Capacity Fade of $\text{LiNi}_{(1-x-y)}\text{Co}_x\text{Al}_y\text{O}_2$ Cathode for Lithium-Ion Batteries during Accelerated Calendar and Cycle Life Test. I. Comparison Analysis between $\text{LiNi}_{(1-x-y)}\text{Co}_x\text{Al}_y\text{O}_2$ and LiCoO_2 Cathodes in Cylindrical Lithium-Ion Cells during Long Term Storage Test. *J. Power Sources* **2014**, *247*, 412–422.

(58) Yoo, J.; Kim, J.; Jung, Y.; Kang, K. Scalable Fabrication of Silicon Nanotubes and Their Application to Energy Storage. *Adv. Mater.* **2012**, *24*, 5452–5456.

(59) Augustyn, V.; Come, J.; Lowe, M.; Kim, J.; Taberna, P.; Tolbert, S.; Abruña, H.; Simon, P.; Dunn, B. High-Rate Electrochemical Energy Storage through Li^+ Intercalation Pseudocapacitance. *Nat. Mater.* **2013**, *12*, 518–522.

(60) Brezesinski, T.; Wang, J.; Tolbert, S.; Dunn, B. Ordered Mesoporous $\alpha\text{-MoO}_3$ with Iso-Oriented Nanocrystalline Walls for Thin-Film Pseudocapacitors. *Nat. Mater.* **2010**, *9*, 146–151.

(61) Zu, L.; Su, Q.; Zhu, F.; Chen, B.; Lu, H.; Peng, C.; He, T.; Du, G.; He, P.; Chen, K.; Yang, S.; Yang, J.; Peng, H. Antipulverization Electrode Based on Low-Carbon Triple-Shelled Superstructures for Lithium-Ion Batteries. *Adv. Mater.* **2017**, *29*, 1701494.